FRAGMENT EMISSION IN ^{32}S+^{197}Au COLLISIONS AT FERMI ENERGY

H. Machner

Fachbereich Physik, Universität Duisburg-Essen, Duisburg, Germany

M. Nolte, M. Palarczyk

Institut für Kernphysik, Forschungszentrum Jülich, Jülich, Germany

T. Kutsarova

Institute of Nuclear Physics and Nuclear Energy, Sofia, Bulgaria

(Received September 20, 2016; accepted July 3, 2017)

Intermediate mass fragment emission from the interaction of sulphur with gold ^{32}S+^{197}Au at a beam energy of 1.01 GeV (31.5 MeV A) was measured at various angles with silicon ΔE–E telescopes. At the most forward angle $\vartheta = 17^\circ$, an additional ΔE detector, an ionisation chamber was used. The measurements were successfully compared with other data of similar systems. Angle integration of cross sections was performed within the generalised moving source model. The isotopic cross sections were compared to theoretical calculations within quantum molecular dynamic and statistical multi-fragmentation models.

DOI:10.5506/APhysPolB.48.1303

1. Introduction

It is well-known that atomic nuclei at low excitation energies deexcite by statistical emission of particles and/or photons. Since this process behaves almost like emission from a hot source having a temperature T, it is also called evaporation. At excitation energies greater than $\approx$ 3 MeV per nucleon, the time intervals between the successive emissions become comparable with the relaxation time $\tau_{\rm rel}$ and usual sequential decay mechanisms may no longer be valid. In this case, one should expect a more or less continuous flux of nucleons and light clusters from a decaying nucleus. At excitation energies comparable with the total binding energy, $E_{\rm B} \approx 5$–8 MeV/nucleon, the very existence of a long-lived compound nucleus becomes unlikely. In this situation, the evaporation-like decay mechanisms

should give way to an explosion-like process leading to the total disintegration of the nucleus and the multiple emission of nuclear fragments of different mass. Thus, the observation of fragments with $Z > 2$ called intermediate fragment emission (IMF) is believed to be the experimental signature of such a scenario. Since the formation of a lot of fragments is typical for a system with the van der Waals forces, this multi-fragmentation process is sometimes called a phase-transition from the dense liquid to a dilute gaseous system. Different models have been proposed being either statistical or dynamical models in order to describe the experiments. There are: statistical multi-fragmentation (SMM) [1, 2], percolation theory [3], Fisher condensation theory [4, 5], quantum molecular dynamics (QMD) [6, 7], Boltzmann–Uehling–Uhlenbeck (BUU) [8, 9] and similar kinetic models, just to name a few.

The above scenario is expected to occur in heavy-ion reactions at Fermi energies. Experimental evidence is multi-fragmentation and emission of IMFs with distributions different from fission fragment distributions. There are numerous experiments with different dedicated detectors. Details can be found in Refs. [10–12] and [13].

Many of these setups have a large acceptance and thus are ideal for large multiplicities. Some of them have moderate isotopic resolution, others with excellent resolution suffer from geometrical acceptance or limited energy acceptance. In the present study, we avoid at least the last point.

In previous studies, we reported on charge correlations for the same system as here [14] or for a system with the same velocity [15]. The finding is that for high energies and small emission angles, the underlying reaction mechanism is projectile break-up with nucleon exchange. In a more recent work, we find that this break-up component shows up only for heavy-target nuclei [16]. For large emission angles and small energies, the emission is statistical. Hence, it is this energy range we have studied in the present experiment.

2. Experiment

2.1. Setup

The experimental setup and the beam properties are almost the same as those described in Ref. [16]; here, we briefly recall them for the sake of completeness. The experiments were carried out at the Jülich isochronous cyclotron which accelerated $^{32}S^{13+}$ ions to 1.01 GeV. Typical beam currents were 0.6 nA when measuring at forward angles and up to 3 particle nA when measuring at large angles. The beam was focused on the centre of the reaction chamber, which allowed measurements at 17°, 35°, 53°, 71°, 89°, and 107°.

The layout of this chamber is shown in Fig. 1. A target ladder in the centre of the chamber carried a self-supporting foil of gold having a thickness of 9.75 μg/cm^2. In addition, a zinc-sulphite foil was mounted serving as

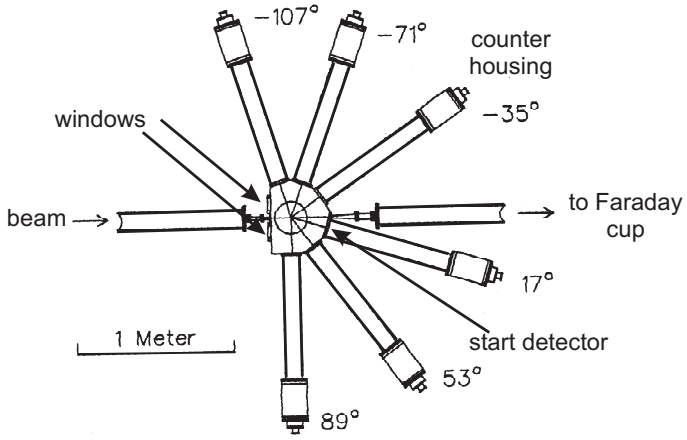

Fig. 1. Layout of the reaction chamber. The boxes at the ends of tubes house the counters. For the measurements at large angles, the tubes were removed to enlarge the solid angle (see Table I).

beam viewer. The beam was focused on this viewer in the centre of the scattering chamber and then dumped 4 m downstream with the help of a pair of quadrupole magnets into an air cooled Faraday cup which measured the charge. Electrons released in the beam dump were pushed back by an aperture connected to a high voltage. Reaction products were detected with telescopes. Those at the two most forward angles consisted of ΔE_1–ΔE_2–E_3 detectors. The ΔE_1 detectors were ionisation chambers discussed below. The ΔE_2 were 5×5 cm^2 Si-diodes of 300 μm thickness (from Micron Semiconductor Ltd). As E_3-detectors we used 4 mm thick Si(Li)-diodes of 6 cm diameter, fabricated in the IKP detector laboratory. At the larger angles, only the silicon counters were used. The solid angles were defined by rectangular apertures made of brass. They are given in Table I.

TABLE I

Geometry of the detectors.

Angle [°]	Opening angle [°]	Solid angle [msr]
17	2.58	2.02
35	2.47	2.07
53–107	7.6	17.7

The diodes were followed by the standard electronics: commercial charge sensitive pre-amplifiers, modified to 4 mV/MeV for the first and 1.9 mV/MeV for the second silicon counters, in the experimental hall and main amplifiers and voltage-dependent ADCs in an electronic room. In the present experiment, both forward detectors operated behind a window (8 μm aluminium coated Mylar) and $\approx$ 5 cm gas of the ionisation chamber. The isotopic separation was therefore limited only up to beryllium. Spectra for fragments up to iron were recorded.

The detectors positioned at 17° and 35° were different from those at the larger angles. Unfortunately, the 35° setup did not become operational so we give here only numbers for the 17° angle. In order to reduce the lower energy threshold of the setup, an ionisation chamber (ΔE_1) of 5 cm length was positioned in front of the first silicon counter (see Fig. 2). It was filled with isobutane at a pressure of 12 kPa or 120 mbar. The electrodes 7 cm apart from each other were almost parallel to the particle trajectories. Close to the anode (2 cm) was a Frisch grid yielding signals independent of the point of ionisation.

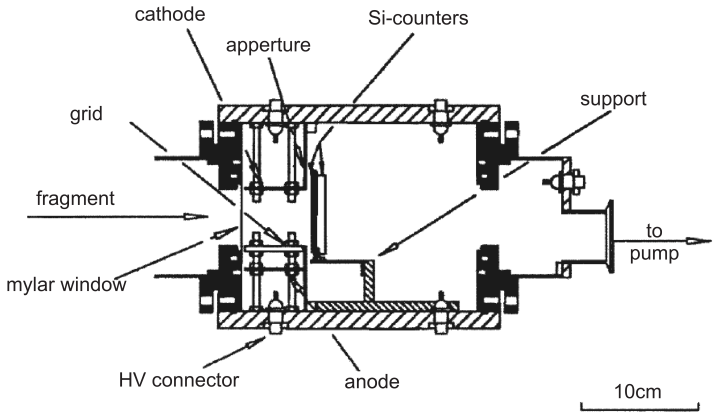

Fig. 2. Layout of the ionisation chamber.

An entrance window consisted of an aluminium coated Mylar foil of 8 μm thickness and a supporting grid. The ionisation chamber was followed by two silicon counters as stated above. These silicon counters were operated inside the gas thus avoiding an additional window. Their support allows to move them backward if a further ionisation chamber will be installed. All these devices were mounted in a box which was positioned at the end of a vacuum tube approximately 1 m away from the target chamber. In our setup for the angles larger than 35°, only the two silicon counters were employed. In order to have a larger solid angle and thus a higher count rate, the long tubes for a time-of-flight measurement were replaced by short ones.

At this point, we want to discuss the setups of other experiments and compare their accomplishments with the present one. The CHIMERA forward detector system consists of ΔE silicon detectors of similar thickness as the present ones followed by CsI(Tl) scintillators. Isotopic separation up to oxygen was achieved with these devices [17]. Although the resolution of silicon detectors is known to be superior to scintillators, the present setup could not reach this quality. The FAZIA Collaboration [18] achieved isotopic resolution up to $Z = 20$ with a first silicon counter of nominal 300 μm and dedicated electronics. However, this advantage is achieved with the disadvantage of missing low-energy particles. The collaboration overcame this problem by applying dedicated electronics allowing pulse-shape analysis for particles being stopped in the first counter [19]. A study of identification properties of a Si–Si ΔE–E telescope exploiting a partially depleted residual-energy detector has been performed [20]. Isotopic separation over a rather large charge range could be obtained. However, the good isotopic resolution comes at the price of somewhat higher charge identification thresholds. Also the long shaping time of tens of μs restricts the counting rate. The Nimrod Collaboration [21] achieved a large dynamical range by Si–CsI and Si–Si–CsI telescopes with silicon counters of 150 μm, 300 μm or 500 μm thicknesses respectively in front of CsI crystals. These counters have much smaller areas compared to those in the present experiment. This resulted in smaller capacitances and therefore in smaller noise. The final result is a much better isotope resolution than the one of the present setup. An ionisation chamber as used here does not allow isotopic resolution with the ΔE–E method. This deficiency can be overcome by an additional time-of-flight (TOF) measurement, which is foreseen for further experiments.

It should be mentioned that the present experiment measures only energy spectra of different elements at different angles. Therefore, the peripheral or central collisions cannot be discriminated. It is truly an inclusive measurement.

2.2. Energy calibration

The energy response of the three detectors was deduced via two complementary methods. First, a precision pulse generator was calibrated with radioactive sources. For the silicon counter ^{244}Cm with an α energy of 5.805 MeV was used. The ionisation chamber was calibrated with a ^{148}Gd source having an α energy of 3.271 MeV. This source was produced by a $^{151}\mathrm{Eu}(d, 5n)^{148}\mathrm{Gd}$ reaction making use of a 50 MeV deuteron beam. In order to avoid self-absorption of the low-energy alpha particles, a thin europium target of only 60 μg/cm^2 was used. In total, 3.375×10^{18} deuterons hit the target leading to a total activity of 6 Bq. Finally, the back side of the otherwise fragile foil was supported leading to only half of the usable

activity. The calibrated pulse signals were fed into the preamplifier circuits simulating different energies. The thickness and pressure of the ionisation chamber were sufficient to stop the alpha particles completely. Thus, the ionisation chamber is at least equivalent to a 13.3 μm silicon layer.

The second calibration method made use of the energy-range method. For the stopping powers, we used the programme SRIM [22] and the tables of [23].

For that purpose, a beam of ^{14}N was used. In Fig. 3, the response of the ionisation chamber (ΔE_1) and the first silicon counter (ΔE_2) is shown. Not shown is the back bending of the hyperbola due to particles reaching the second silicon counter. The points and the corresponding energy points in the ionisation chamber are shown by arrows. From these measurements, we find that the ionisation chamber is equivalent to a 15 μm silicon layer. In Fig. 4, we show the response of the same counters for the present reaction. Fragments up to iron are detected although with poor statistics. The charge resolution is much better for higher energies employing the second and third counter as is shown in Fig. 5. Here, one can select even ^{7}Be from the other beryllium isotopes, because of the non-existence of ^{8}Be.

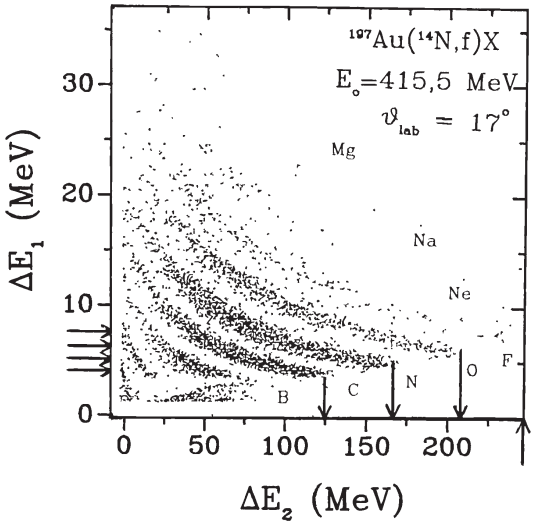

Fig. 3. The response of the ionisation chamber (ΔE_1) *versus* the first silicon counter (ΔE_2) as a scatter plot from a nitrogen beam hitting on the gold target. The arrows indicate the energies deposited in the counters for the particles stopped with maximal energy in the silicon counter. The different elements are indicated next to the appropriate hyperbola.

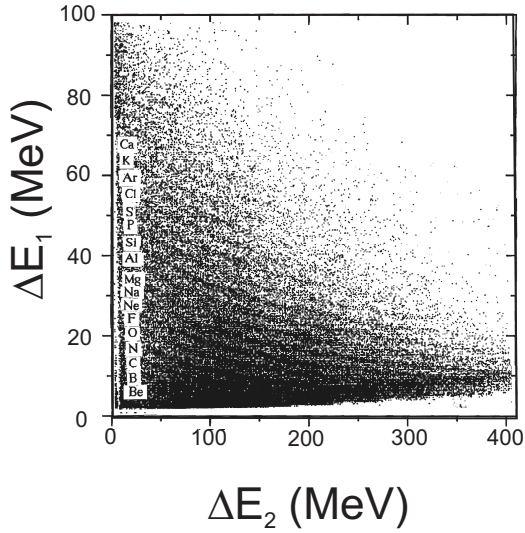

Fig. 4. The same as Fig. 3 but for the sulphur beam and reduced amplifications. Particles can be identified up to calcium.

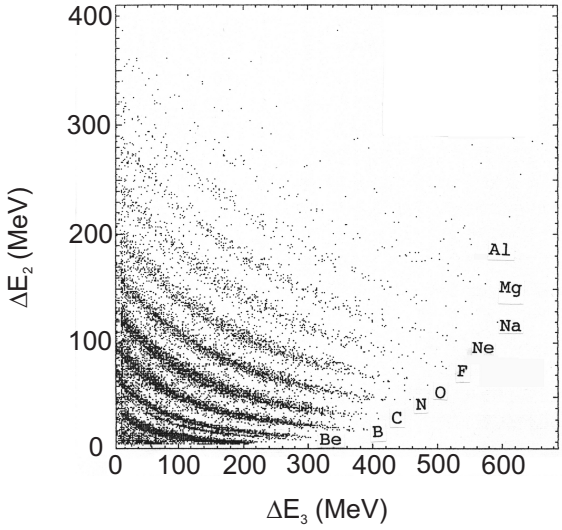

Fig. 5. The same as Fig. 4 but for ΔE_2–ΔE_3 plot measured with two silicon counters.

2.3. Energy spectra

Cross sections were deduced from the count rate, target thickness, solid angel opening and beam flux. At $\vartheta = 17°$, the lowest energy is given by the thickness of the ionisation chamber, at angles 53°, 71°, 89° and 109°, the lower threshold is due to the 300 μm silicon counter. In Fig. 6, we show the double differential cross sections for lithium fragments as a function of the different laboratory angles. Spectra from [24, 25] for the similar reaction ^{40}Ar+^{197}Au at close angles are also shown. They compare favourably with the present results. Also shown are fits with the generalised moving source

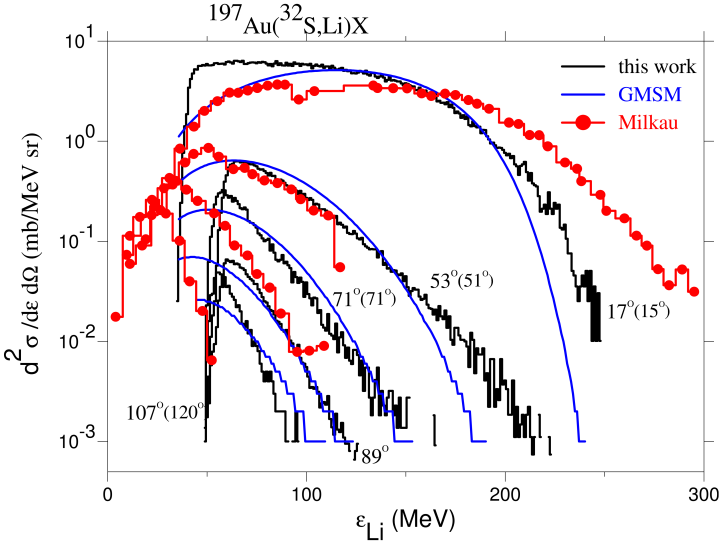

Fig. 6. (Colour on-line) Energy spectra of lithium for the emission angles indicated in the figure. The results from the present experiment are shown as histograms (black), those from [24, 25] for the ^{40}Ar+^{197}Au as histograms with points (red). The angles for the latter are given in brackets. The solid curves (blue) represent the results of the GMSM (see Section 2.1).

model (GMSM) [26, 27] which is discussed further down. Finally, we present double differential cross sections for all detected charges at the angle 17° in Figs. 7 and 8. The spectra are smooth curves with a structure, which will be discussed further down.

In principle, the spectral shape and also the total yield can be influenced by a reduced efficiency. This originates for the fragment energies of the present reaction mainly from nuclear absorption in the detector material. We apply the model of Ref. [28] to estimate the efficiency. The energy dependence of the efficiency for some selected fragment types is shown in Fig. 9. The shown range is truncated to concentrate on the range of energies

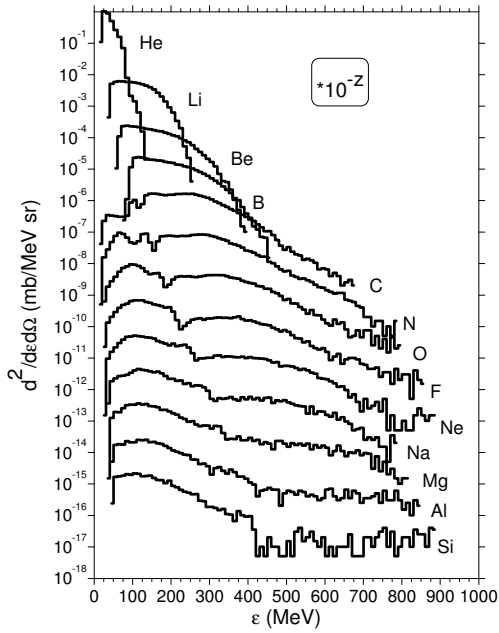

Fig. 7. Energy spectra for the indicated fragment elements. In order to have a good visibility of the data, the height was scaled by successive factors of 10.

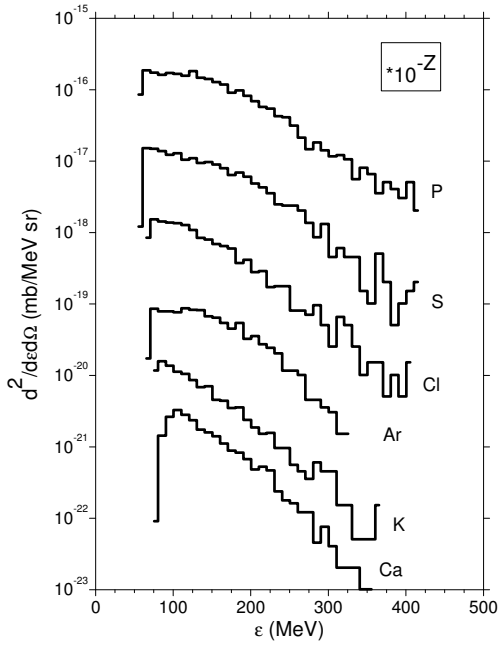

Fig. 8. The same as Fig. 7 but for fragment charges 15–20.

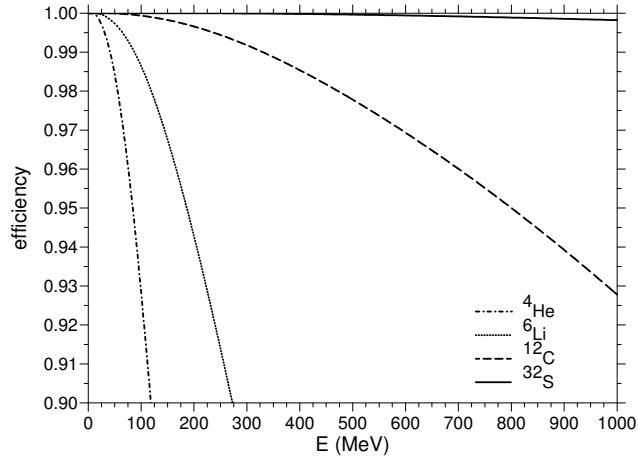

Fig. 9. The efficiency of Silicon counters as a function of the energy for different fragments indicated in the figure.

of the fragments in the present experiment shown in Figs. 7 and 8. The efficiency is much larger for the heavy ions than for light ions [28]. This is an outcome of the larger Coulomb barrier for heavy ions compared to light ions. The only spectrum where the reduced efficiency may have an effect is lithium. In Fig. 10, we show the uncorrected and efficiency-corrected spectra at $\theta = 17°$. The correction has a very small effect on the cross

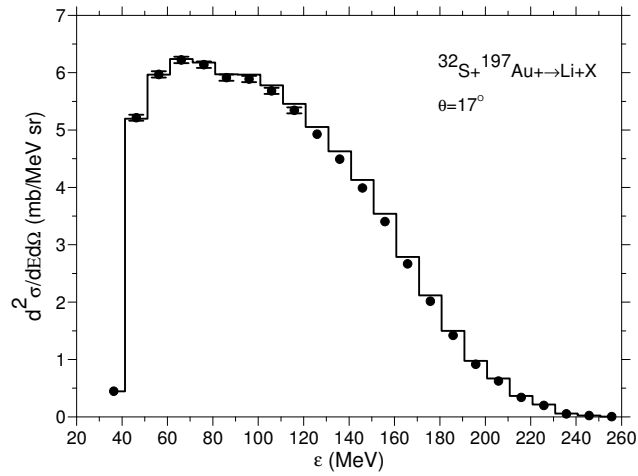

Fig. 10. The energy spectrum of lithium ions at the indicated laboratory angle. The data before correction are shown as dots with error bars, efficiency corrected as histogram.

section around $\epsilon = 150$ MeV. The total cross section changes by less than 2%. For helium the effect is less than 4‰. So in the following, we will ignore efficiency corrections.

At this point, we will discuss the structure visible in the spectra. If the origin of this structure were a threshold in the electronics, it would be always at the same energy, independently of the fragment type, because the electronics is highly linear. In order to check the origin of the structures, we have studied the differential cross sections as a function of the fragment range in the 17° telescope. Examples for oxygen, neon and magnesium are shown in Fig. 11. There are always minima around 250 μm which most

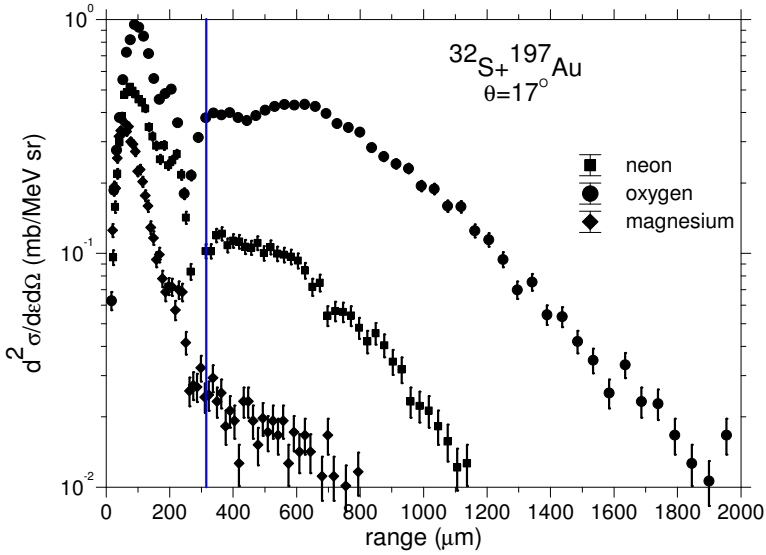

Fig. 11. The 17° cross sections for oxygen, neon and magnesium as a function of the range in silicon. The line is the border of the ΔE_1–ΔE_2 telescope.

probably occurs because in the ΔE_2 counter with 300 μm thickness is not fully depleted due to a too small bias voltage. In order to check the amount of missing yield, we have fitted smooth curves to the spectra as a function of energy by excluding ranges from 150 μm to 330 μm, which corresponds to exclude the energy region between 146 MeV and 216 MeV for O, 190 MeV and 226 MeV for Ne, and 246 MeV and 396 MeV for Mg, as is shown in Fig. 12 as open points (see the caption). We can now compare the energy integrals of the experimental data and the fits. This comparison shows that the experimental cross sections are reduced by 5.3%, 3.4% and 1.1% for oxygen, neon and magnesium, respectively. In summary, the experiment has a slightly reduced cross section in the range which is measured by the ΔE_1–ΔE_2 telescope by a few percent.

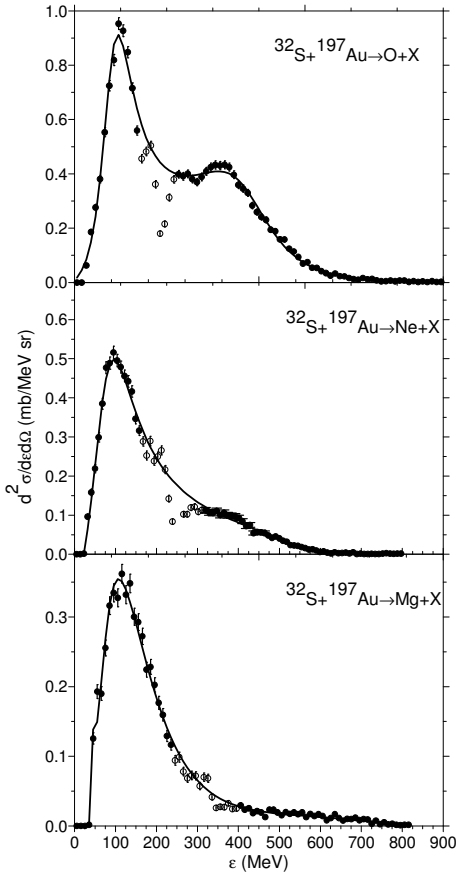

Fig. 12. The same as Fig. 11 but as a function of the energy. The experimental data are shown as dots with error bars. The points included in the fits are shown as full dots, those excluded in the fits are shown as open dots.

2.3.1. Comparison with other experimental results

To our knowledge, the only previous study of the present reaction was given by Lleres *et al.* [29] using the sulphur beam from the SARA accelerator at Grenoble. Their telescope was somewhat similar to the present ones: ionisation chamber followed by silicon counters. Measurements which are closely related to the present one are from Milkau [24, 25] and Kim *et al.* [30]. Milkau used also a beam from SARA, but ^{40}Ar at 30 MeV per nucleon. Again, they used a telescope of the type ionisation chamber plus three silicon counters of 50 μm, 500 μm and 1000 μm, and a BGO scintillator. At the most forward angle (15°), the ionisation chamber was missing. Kim *et al.* used a ^{36}Ar beam from the $K = 500$ MSU cyclotron and particle detection was

made with some rings of the MSU miniball [10]. The individual telescopes were thin plastic scintillator followed by CsI scintillator. Common to all experiments is the fact that only charge resolution was achieved. In the following, we will compare some energy spectra from the present experiment with those from the three older ones.

The first comparison for the rather light element lithium is done in Fig. 6 for a large angular range with data from Milkau [24, 25]. There is a good agreement with respect to absolute height as well as spectral shape. The same is true for the most forward spectrum of beryllium fragments (see Fig. 13). The level of agreements over a large energy range is remarkable. Kim *et al.* [30] report the spectra only as probability distributions. In order to achieve cross sections, we have multiplied their values by the geometrical cross section. With 20° we denote the angle which is in the vicinity of this value. For the present data it is 17°, for those of [24, 25] it is 15°, for those of [29] it is 20°, and for those of [30] it is 19.6°. Similarly, we write for the projectile energy 30 MeV A although the different experiments have slightly different bombarding energies.

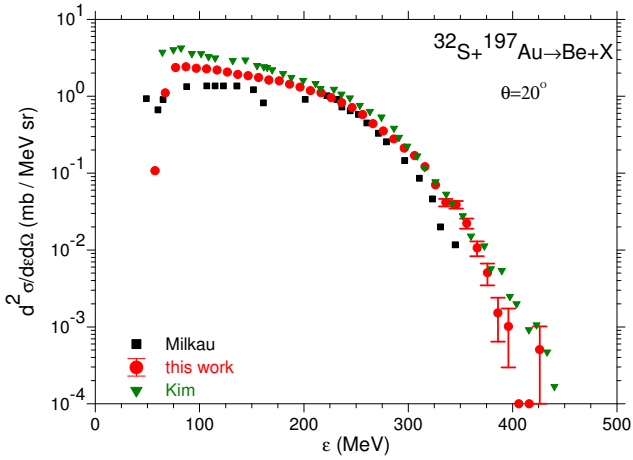

Fig. 13. (Colour on-line) Energy spectra for the emission of beryllium at approximately 20°. The present data are plotted as full dots (red), those of [24, 25] as squares (black) and those from [30] as inverted triangles (green).

We now proceed comparing energy spectra for fragments having larger charge numbers. Spectra for oxygen fragments are shown in Fig. 14. Now, the spectrum from [30] falls off steeper than the present data. The Milkau data are in agreement with the present ones although not extending to the high energies. The cross sections reported by [29] are somewhat larger than the others. It should be mentioned that our previous measurements [16] on silver agree nicely at all angles with those of [29].

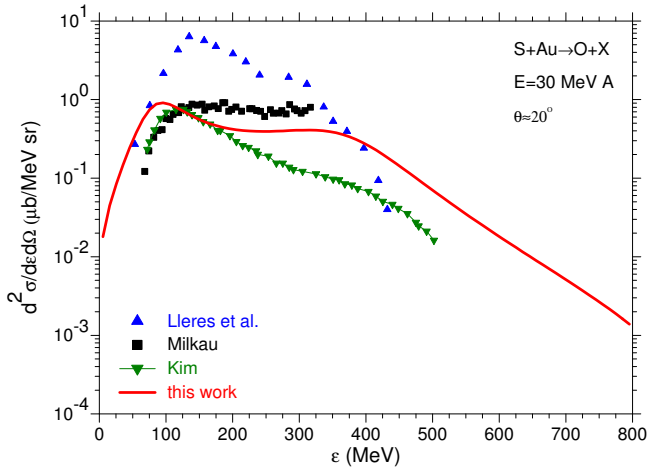

Fig. 14. (Colour on-line) The same as Fig. 13 but for oxygen fragments. In addition, data from [29] are shown as triangles (blue). The curve indicating the present work is the fit shown in Fig. 12.

For fragments with even larger charge numbers, the influence of different projectiles shows up. In such cases, we compare the spectra on the basis of the same number of removed charges $\Delta Z = Z_\mathrm{p} - Z_\mathrm{f}$, were Z_p is the projectile charge and Z_f is the fragment charge. So for the present system, a silicon fragment denoted 'Si' corresponds to $\Delta Z = 2$. We then compare it with the Milkau data from argon-induced reaction with sulphur fragments for which, again, $\Delta Z = 2$ holds. Although the velocity of the projectiles or the energy per nucleon are quite similar, the total energies are not. We therefore compare heavier fragments on the basis of energy per fragment ε/Z_f. This is done in Fig. 15 for fragments ranging from neon to silicon. The present spectra show at low energies of 10 MeV per charge an evaporation-like maximum and then an exponential fall off. The Milkau spectra (magnesium to sulphur in reality) show the same. There is a remarkable agreement between the present data and those of Milkau with respect to the absolute height and shape in the lower energy range. The bump at beam velocity, corresponding to $\varepsilon/Z_\mathrm{f} \approx 60$ MeV, of the latter is strongly increasing with the fragment charge number, a feature not visible in the present data. It can be understood if argon has a larger probability to break-up into fragments than sulphur. Also shown are spectra from Lleres *et al.* [29] where available. The energy range is smaller than the other measurements. These cross sections have the tendency to be larger than those of the other data sets. They seem to be considerably large and independent of the fragment charge number, which is in contrast with their cross sections from the silver target.

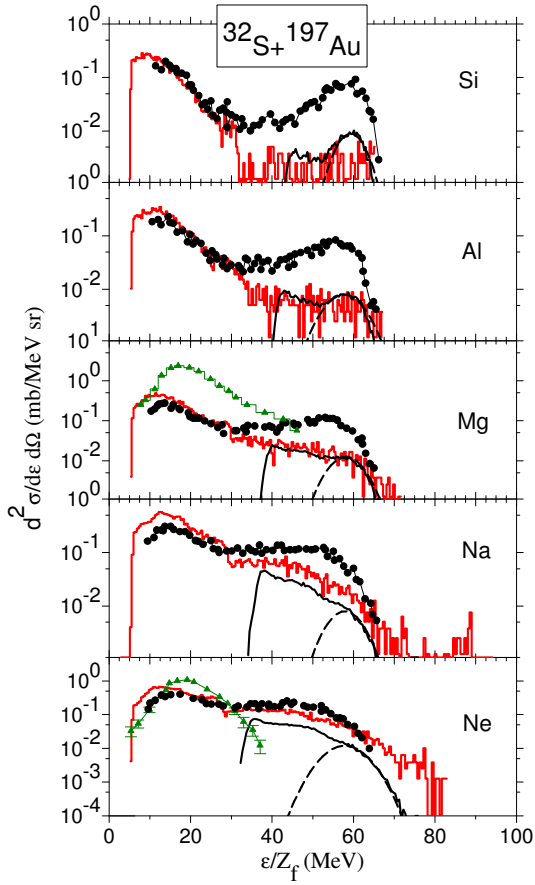

Fig. 15. (Colour on-line) Comparison of energy spectra at angles close to 20° (see the text). The present data are shown as histograms (red), those from Milkau [24, 25] as dots (black). The data shown by triangles (green) are from [29]. Data from a uranium target [16] are plotted as solid curves (black). The dashed curves (black) are Gaussian fits to the high-energy part of the later spectra. See the text for choice of fragments in case of data from Milkau.

Also shown in the figure are the cross sections from the reaction ^{32}S+^{238}U [16] in the same beam energy range as the present results. In these measurements, the ionisation chamber was missing and hence the energy range 10–30 MeV/Z_f is lacking. There is a nice agreement between the two measurements in the overlap range. Also shown are Gaussian fits to the high-energy parts of the spectra.

2.4. Energy integrated cross sections

We now proceed and integrate numerically the double differential cross sections $\mathrm{d}^2\sigma/\mathrm{d}\Omega\mathrm{d}\epsilon$ over the energy and obtain differential cross sections $\mathrm{d}\sigma/\mathrm{d}\Omega$. These are shown in Fig. 16 as a function of the fragment charge. There is some structure for $Z \leq 10$ over a general trend which falls off exponentially. After a steep decrease from helium on, a local minimum for $Z = 4$ shows up. This is most probably due to the particle unstable isotope ^{8}Be. A maximum is visible for carbon. We have fitted two exponentials to the distribution with slope parameters -2.60 ± 0.38 and -0.236 ± 0.013. Also a power law $\mathrm{d}\sigma/\mathrm{d}\Omega = 12947\, Z^{-2.33}$ nb/sr was fitted to the data which is less favourable than the exponentials. All fits are also shown in Fig. 16.

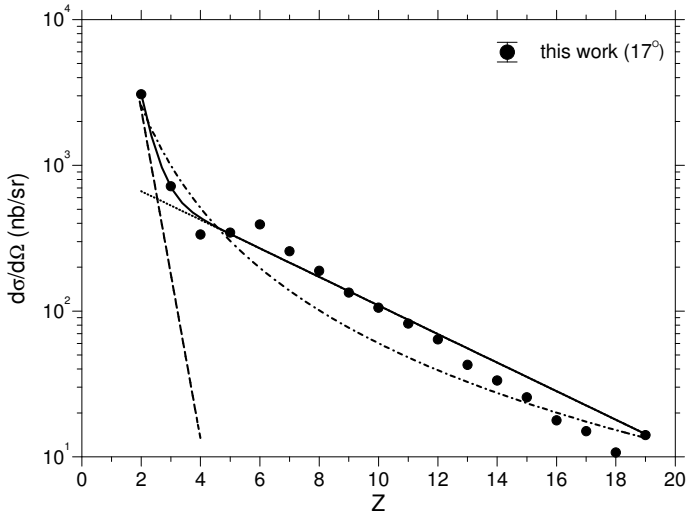

Fig. 16. (Colour on-line) The energy-integrated cross sections at $\vartheta = 17°$ as a function of the fragment charge number Z. A fit with two exponentials is also shown (solid curve). The two components are also shown separately: the small charge component as long-dashed curve, the one for heavier charges as dotted curve. The dash-dotted curve indicates a power law fit.

2.5. Total yields

We calculate total cross sections from the differential cross sections by applying the generalised moving source model (GMSM) [26]. Instead of assuming different moving sources with different source velocities and temperatures, the model assumes a series of sources so that the source velocity and temperature become continuous functions of the emission energy. This model thus includes an implicit dependence on the impact parameter. Large

impact parameters lead to peripheral reactions and therefore to projectile-like fragments with velocity close to the beam velocity. Smaller impact parameters lead to more energy transfer from the projectile to the target and to more nucleon exchange. Central collisions lead to the formation of a composite from projectile and target with signature of small fragment energies. Within this model, the differential cross section is assumed to follow the relation

$$\frac{\mathrm{d}^2\sigma(Z,\theta,\epsilon)}{\mathrm{d}\Omega\epsilon} = C\sqrt{\epsilon}\exp\left[-\left(\epsilon - \sqrt{2m\epsilon}v(\epsilon)\cos\theta + \tfrac{1}{2}mv(\epsilon)^2\right)/T(\epsilon)\right], \quad (1)$$

where C is a normalisation constant, m is the mass of the fragment, v denotes the velocity of the source and T its temperature. This leads to

$$\ln\frac{\mathrm{d}^2\sigma(Z,\varepsilon,\vartheta)}{\mathrm{d}\varepsilon\mathrm{d}\Omega} = b(Z,\varepsilon) + a(\varepsilon)\cos(\vartheta) \quad (2)$$

for a constant ejectile energy, with

$$b(\epsilon) = \ln\left(C\sqrt{\epsilon}\right) - \left(\epsilon + \tfrac{1}{2}mv^2\right)/T \quad (3)$$

and

$$a(\epsilon) = \frac{\sqrt{2m\epsilon}v}{T}. \quad (4)$$

In Ref. [16], $a(\varepsilon)$ was extracted from fragment spectra from sulphur-induced reactions at the same energy as the one applied in this work. A few points extracted from the present measurements are shown in Fig. 17 together with the earlier result from [16]: $a(\varepsilon) = 1 + (0.006677 \pm 0.000223)\varepsilon^{3/2}$. These values nicely agree with the previous finding.

In previous studies, we were interested in reproducing the spectral shapes. For that purpose, we fitted $T(\epsilon)$ and the normalisation constant C to the data by assuming a polynomial

$$T(\epsilon) = \sum_{i=0}^{i_{\max}} t_i\epsilon^i. \quad (5)$$

We found $i_{\max} = 1$ similar as in Ref. [16] to reproduce the data. An example for the data here is given in Fig. 6. However, for further discussion, we need to know total cross sections. We, therefore, deduce angle integrated cross section within the GMSM.

Angle integration leads to [31]

$$\begin{aligned}\frac{\mathrm{d}\sigma(Z,\varepsilon)}{\mathrm{d}\varepsilon} &= \frac{2\pi}{a}\left(e^{b+a} - e^{b-a}\right)\\ &= \frac{4\pi}{a(\varepsilon)}\frac{\mathrm{d}^2\sigma(Z,\varepsilon,\vartheta)}{\mathrm{d}\varepsilon\mathrm{d}\Omega}\frac{\sinh[a(\varepsilon)]}{\exp[a(\varepsilon)\cos(\vartheta)]}.\end{aligned} \quad (6)$$

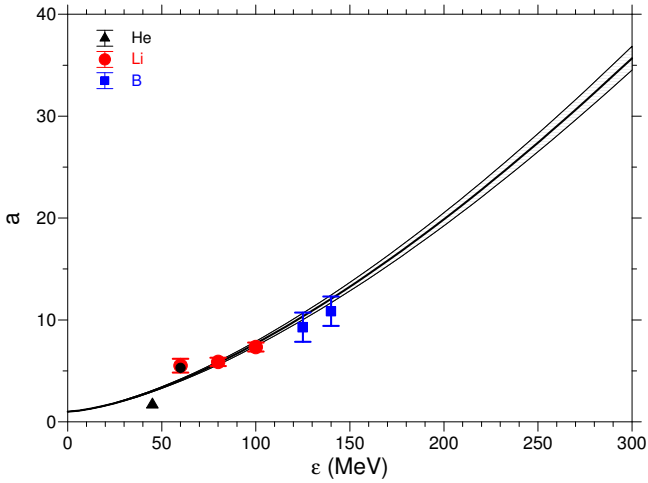

Fig. 17. (Colour on-line) The energy dependence of the parameter a as obtained from the interaction of sulphur at the same bombarding energy as our reaction with targets of vanadium, silver and uranium [16] is shown as a solid curve with error band (black). Some results from the present measurement are shown as symbols with error bars: helium as up triangles (black), lithium as full dots (red) and boron as full squares (blue).

Since $\exp(-a) \ll \exp(a)$, a good approximation is

$$\frac{\mathrm{d}\sigma(Z,\varepsilon)}{\mathrm{d}\varepsilon} \approx \frac{2\pi}{a(\varepsilon)} \frac{\mathrm{d}^2\sigma(Z,\varepsilon,\vartheta)}{\mathrm{d}\varepsilon \mathrm{d}\Omega} \exp\left[a(\varepsilon)(1-\cos(\vartheta))\right] . \tag{7}$$

Making use of the experimental double differential cross sections

$$\mathrm{d}^2\sigma(\varepsilon, 17^\circ)/\mathrm{d}\varepsilon \mathrm{d}\Omega$$

and the energy dependence of $a(\varepsilon)$, we obtain the differential cross sections for a fragment charge Z $\mathrm{d}\sigma(\varepsilon, Z)/\mathrm{d}\varepsilon$. Then the differential cross section is summed up to get the total cross section $\sigma(Z)$.

These cross sections are shown as a function of the charge number in Fig. 18. The general behaviour of the differential cross section $\mathrm{d}\sigma/\mathrm{d}\Omega$ (see Fig. 16) remains: strongly decreasing with increasing charge number with a strong minimum around $Z = 4$. A second local minimum shows up around $Z = 18$. Also shown are the total cross sections from Lleres *et al.* [29] for the same reaction and from Milkau [24, 25] for the ^{40}Ar induced reactions. Also these data show the same general trend as the present data. The increase of cross section for $Z > 18$ is due to the onset of fission events as will be discussed in connection with the PHITS calculations further down.

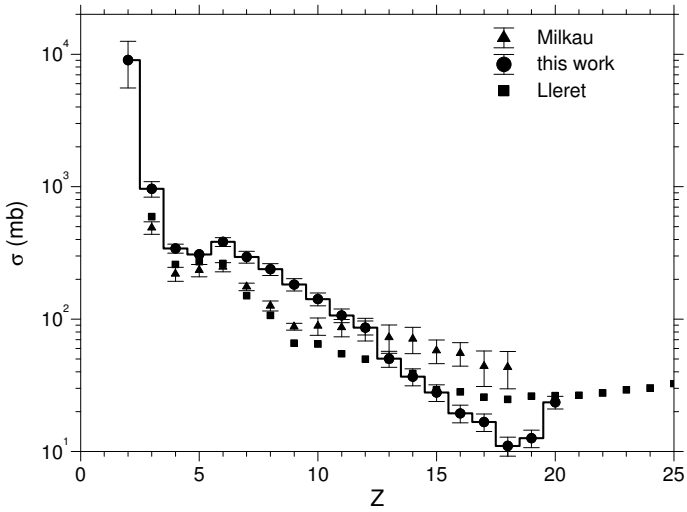

Fig. 18. Total cross sections as a function of the charge number Z. The present experimental results are shown as full dots with error bars connected by a histogram. The results from Milkau [24, 25] are shown by triangles with error bars and those from Lleres *et al.* [29] by full squares.

3. Comparison with models

3.1. Odd–even staggering

In this section, we will investigate a possible odd–even staggering of the total cross sections. From the experimental charge distribution in Fig. 18, it is not easy to see such an odd–even effect, since the distribution has a strong decrease at low Z numbers, and minima and maxima. In order to account for odd–even effects with maxima for even nuclei, we have fitted

$$\sigma(Z) = a_0 \exp(-a_1 * Z) + |a_2| \cos(\pi Z) \tag{8}$$

to the data. The uncertainty in a_2 is larger than the fitted value itself. Because the second term is negligible for small values of Z, we have tried a factor $|a_2|/Z$ instead with the same result. Also an assumed pre-cosine factor $\ln[a_0|\exp(-a_1 Z)]$ yields the same χ^2 value as the other choices or the pure exponential. We then proceed and followed the method of D'Agostino *et al.* [32] and Casini *et al.* [33], which is a parabolic fit to five consecutive cross section values to derive a smoothed number for the middle value σ_{smooth}. We then look at the ratio

$$R = \frac{\sigma_{\text{exp}}}{\sigma_{\text{smooth}}}\,. \tag{9}$$

This ratio is shown in Fig. 19 as a function of the charge number. If one ignores the error bars, there is indeed an odd–even staggering effect, *i.e.*

$R > 1$ for even charge numbers and $R < 1$ for odd charge numbers, except for $Z = 4$. However, within error bars, all ratios are compatible with $R = 1$. Inspection of the energy spectra in Fig. 15 indicated that the largest fraction of the cross sections is due to evaporation from an equilibrated source. Since such a system is believed to have "forgotten" how it was formed, one should not expect to see small effects like odd–even staggering.

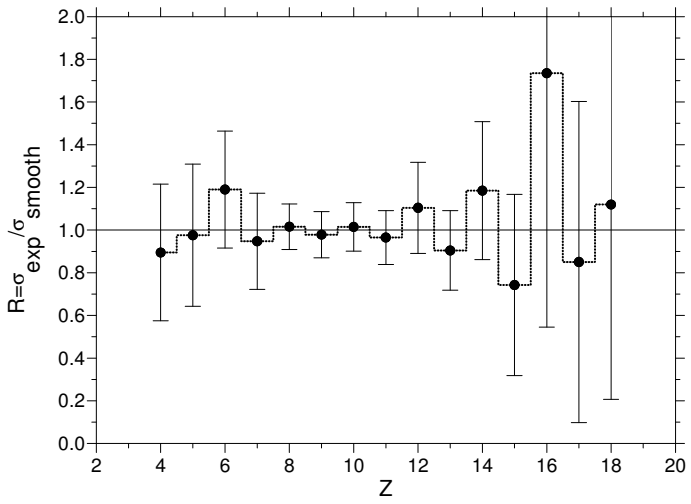

Fig. 19. Ratio (9) as a function of the fragment charge number (see the text).

3.2. Statistical multi-fragmentation model

The statistical multi-fragmentation model (SMM) [1, 2] assumes that the thermalised residual nucleus of the first stage of the projectile nucleus collision undergoes a statistical breakup. At first, the nucleus expands to a certain volume and then breaks up into nucleons and hot fragments. A short summary of the model is given in [16]. For the calculations, we used a code from Ref. [34]. In order to derive an estimate for the excitation energy, we assume energy and momentum conservation. So the energy and the linear momentum of the projectile nucleus is transferred to the system consisting of target plus projectile. This yields an excitation energy of 3.8 MeV per nucleon which is the input of the calculation. One result of the calculation, *i.e.* the charge distribution is compared to the experimental results in Fig. 20. Since the calculation is only on a relative base, we have multiplied them to reach the experimental cross sections. Since the code predicts no absolute cross section, we have multiplied the output with a factor of 400. The predicted slope is flatter than the experimental one. This is similar to the previous study for the uranium target [16]. One reason for the devia-

tion between data and model calculation might be the missing decay of low excited residual nuclei. The authors of the computer code suggest to add a code treating the statistical emission and fission of the final nuclei. We will come back to this point later.

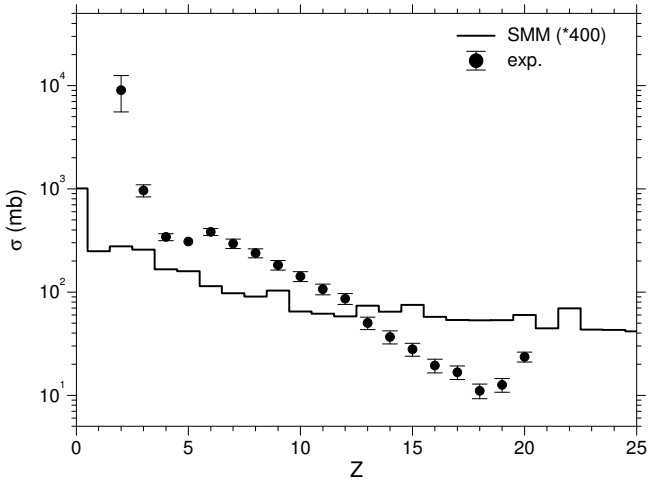

Fig. 20. Comparison of total yields from the present experiment (dots) with a SMM calculation (histogram)

Although the model does not give yields comparable with experimental ones, it is interesting to look at model predictions. One such result are the excitation energy of the fragments and their temperature. So, each fragment can be treated as a compound nucleus. Then a simple estimate of the equation of state (EOS) derived for a Fermi gas is [35]

$$E = \frac{\pi^2}{6} g T^2 - T \,. \tag{10}$$

For sufficiently high energies which is the case for the present system, the linear term can safely be neglected. The quantity $g = 1/d$ is the level density and d the mean distance of levels. It is common to summarise the factors in front of the quadratic term into $\pi^2 g/6 = a$, the level density parameter. Then the EOS reads

$$E = aT^2 \,. \tag{11}$$

From experiments, one finds $a = A/c$, with c the inverse level density parameter, increases with A [36] except for nuclei with closed shells. From the SMM calculation, we can extract the parameter $a = E/T^2$ which is shown in Fig. 21 as a function of the mass number. Similar to the low-energy results and counting of resonances, we find almost linear increase of a with A.

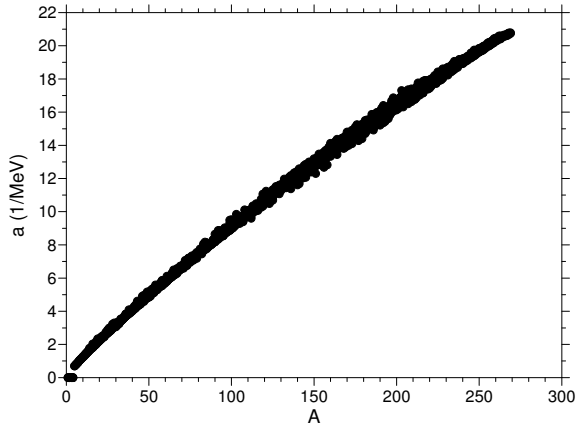

Fig. 21. The mass dependence of the level density parameter a from SMM calculation.

Shlomo and Natowitz [37] studied the temperature dependence of the c parameter. They found an increase of c from 8 MeV for $T = 1$ MeV towards $c = 16$ MeV for $T = 10$ MeV with an S shaped curve. We extract the temperature dependence of c which is shown for the SMM calculation in Fig. 22.

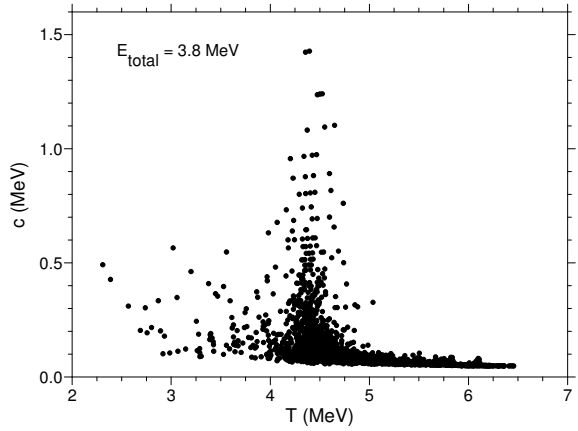

Fig. 22. The temperature dependence of the inverse level density parameter c from SMM calculation.

The extracted points scatter around with some high density for T in the region of 4–5 MeV. It seems that $c(T)$ decreases instead of increasing. From this finding, two conclusions can be drawn: first, c is for the high energy here compared to a compound nucleus much smaller and, therefore, the average level distance d is much smaller. Second, the A dependence indicates that the levels are more dense in heavy nuclei than in light nuclei.

Another quantity which can be derived from the SMM calculation is the caloric curve. This is the temperature of a fragment as a function of the excitation energy per nucleon in the fragment. This curve is shown in Fig. 23. One can identify regions with different behaviour. On the one hand, there is a continuous curve with increasing temperature with increasing excitation energy per nucleon. In addition, there is a region in the middle of the energy range where the temperature is almost constant. Such a behaviour is expected for a first order phase transition. Since the nucleon–nucleon interaction looks like a van der Waals force, one can expect the temperature dependence to follow a phase transition from a liquid to vapour. So at low energies, one expects a liquid, *i.e.* a Fermi gas behaviour (11) while at high energies, the dependence should follow the one of a classical gas $E = 3/2kT$. In the middle, there is a range connecting the two phases. We have fitted dependencies $T = 0.6$ MeV $+3.7\sqrt{E/A}$ for $E/A < 1.5$ MeV and $T = 2.2$ MeV $+4/3E/A$ for $E/A > 2.5$ MeV. The additional events correspond to the boiling liquid with a constant temperature of 4.5 MeV. It is possible to separate the events in two disjoint groups with a condition on the fragment multiplicities: $T \approx$ constant for multiplicities $m \gtrapprox 0.003$ and for the temperature-dependent group $m \lessapprox 0.003$.

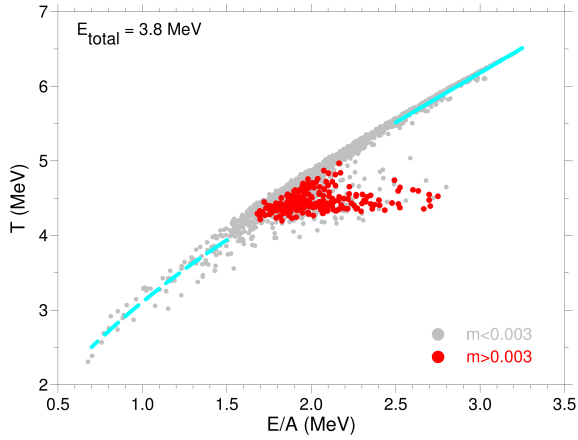

Fig. 23. (Colour on-line) Caloric curve for fragments with multiplicity < 0.003 (grey points) and $\gtrapprox 0.003$ (dark grey/red points). Also shown are fitted curves (black/light blue) $T = 0.6$ MeV $+3.7\sqrt{E/A}$ for $E/A < 1.5$ MeV (dashed) and $T = 2.2$ MeV $+4/3E/A$ for $E/A > 2.5$ MeV (solid).

The border of $m = 0.003$ corresponds to 1.2 mb, which is outside the range in Fig. 20. It is interesting to check from which part of the table of isotopes the fragments within the four ranges, which are identified in Fig. 24, have their origin. Of course, the most frequent fragments are from

light isotopes, which are also indicated in Fig. 24. It is interesting to note that these fragments are more neutron rich than the stable isotopes which are also indicated in the figure. The fragments in the liquid branch are neutron deficient, those in the gas branch are at the most neutron deficient band at the valley of stability.

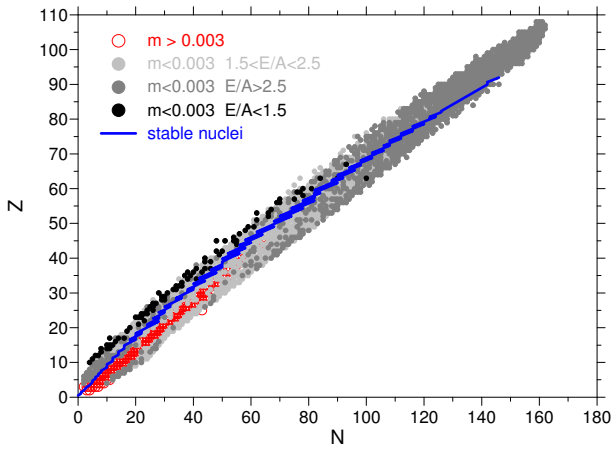

Fig. 24. (Colour on-line) The positions of the different fragments with respect to energy and multiplicity m within the table of isotopes. The (black/blue) curve indicates the stable isotopes.

We have checked the present results by changing the total excitation energy. The middle branch with a constant temperature vanishes from $E_{\text{total}} =$ 14 MeV/nucleon and the temperature becomes proportional to E/A.

3.3. Quantum molecular dynamics

The quantum molecular dynamics (QMD) model is closely related to the Boltzmann–Uehling–Uhlenbeck equation, which is also called the Vlasov–Uehling–Uhlenbeck, Boltzmann–Nordheim or Landau–Vlasov equation, or BUU/VUU approach [38]. Scattering of nucleons is treated within a potential well. Collision and potential term are generated by the same bare interactions (which coincide in a classical theory) and the Fermi statistics. The nucleons are approximated by Gaussian wave packets. The n-body density is a product of n Gaussians. They are interacting with each other through effective interactions as in a framework of molecular dynamics. One can estimate yields of emitted light particles, fragments and of excited residual nuclei. The predictions of the QMD model were obtained with the code PHITS [39–41]. The QMD simulation describes a dynamical stage of nuclear reactions. At the end of the dynamical stage, one gets excited nuclei

from these simulations. In order to get final observables, these excited nuclei should decay in a statistical way. Evaporation and fission of the excited residual nucleus are obtained applying an evaporation code [42]. The prediction of this model for the present system of target and beam is shown in Fig. 25. For small masses, a steep decrease of the yield with increasing charge number shows up. For heavy fragments with high Z, an almost bell shaped structure indicates remnants of the fused system. In the middle around $Z = 40$, a bump represents fission products as it was found by switching off the emission from an equilibrates system.

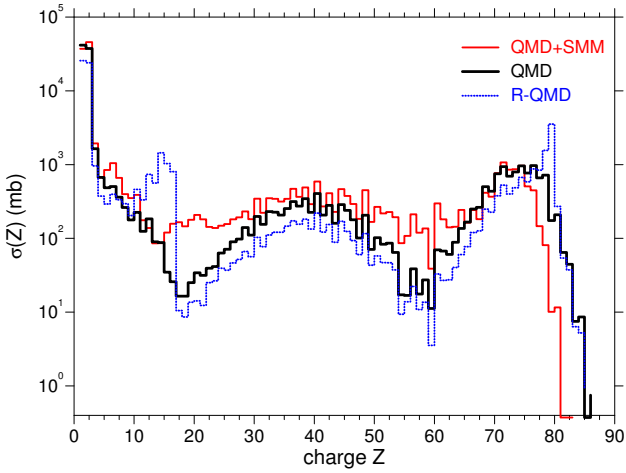

Fig. 25. (Colour on-line) Predictions of the QMD plus evaporation approach (labelled QMD, thick black histogram) and one which includes also an additional SMM step (labelled QMD+SMM, thin grey/red histogram). Also shown is a calculation with a covariant version of the QMD model (labelled R-QMD, dotted blue histogram). All calculations have been multiplied by a factor of five.

In a new version of the code, the SMM was incorporated [43]. If after the QMD calculation the energy per nucleon is below 2 MeV, the calculation is as before. If the excitation energy is above 2 MeV, the SMM (see previous section) is invoked and, finally, the evaporation-fission calculation starts. In Fig. 25, we compare the predictions of the QMD plus evaporation approach with those including an intermediate SMM step. Both calculations show common features. Obviously, the SMM part adds yield to the range around $Z = 18$.

Another option in the entrance channel is the relativistic version of the QMD model [44]. This model adds a fully covariant approach to molecular dynamics. Furthermore, a new ground-state initialisation algorithm for nuclei is added. Calculations with this choice are labelled R-QMD and are

also shown in Fig. 25. The only serious difference between the previous two calculations and this one is in the region $10 \lessapprox Z \lessapprox 35$. While the QMD plus evaporation (QMD) calculation has a minimum at $Z = 18$, the QMD plus SMM plus evaporation (QMD+SMM) calculation has a maximum at $Z = 14$. Fortunately, the present experiment has delivered data in this region where the three calculations disagree with each other. Thus, a confrontation of the calculations with data will allow to draw definite conclusions. Therefore, we compare data and calculations with each other in Fig. 26. With a factor of five the calculations were brought to the height of the data. Obviously, the cross sections for helium emission is now overestimated. We will come back to this point. The experimental cross sections were nicely reproduced by the QMD calculation, while there is disagreement with the QMD+SMM calculation. The latter fills the gap between the exponential decreasing part and the rise of fission yield. The enhancement aground nitrogen predicted by the relativistic covariant approach is also not visible in the data.

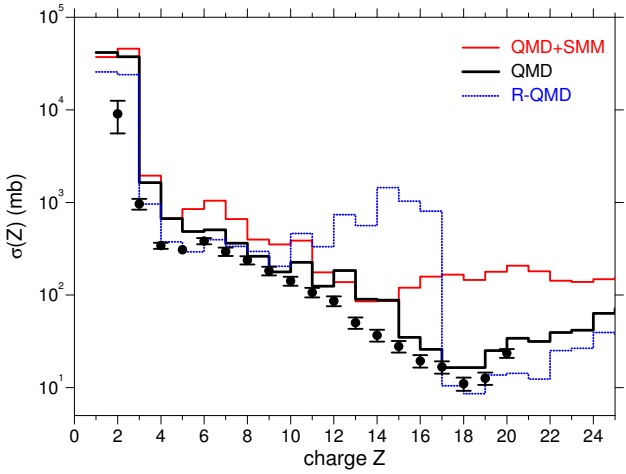

Fig. 26. (Colour on-line) Comparison of the present data (dots with error bars) with PHITS calculations. The calculation employing QMD plus compound nucleus decay is shown as thick black histogram, the one with an additional SMM step is shown as thin grey/red line. The relativistically covariant approach is shown as dotted blue line. The calculations have been multiplied by a common factor of five.

We will now compare double differential cross sections with the PHITS calculation.

This is done for fragments ranging from ^{4}He, lithium, boron to neon for $\vartheta = 17°$ in Figs. 27, 28 and 29. In these calculations, the normalisation factor of five is ignored. In the case of ^{4}He, the calculation agrees favourably with the data. However, for the heavier fragments, the calculations fail to

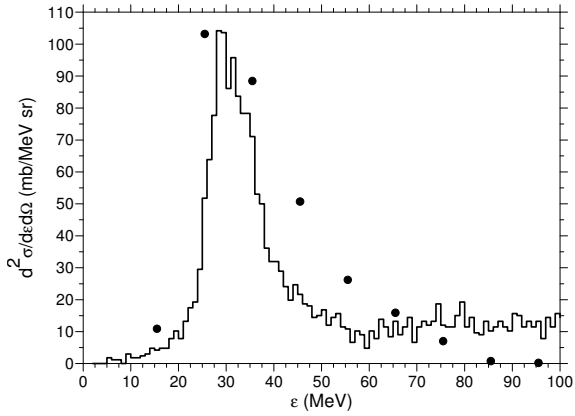

Fig. 27. Comparison between the energy spectrum for helium measured at 17° (full dots) with QMD calculation with the PHITS code for ^{4}He (histogram).

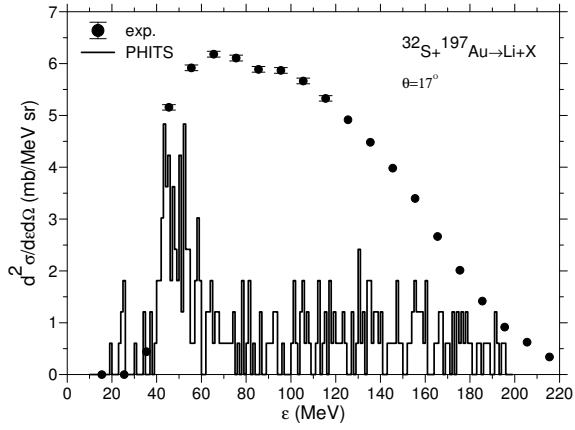

Fig. 28. The same as Fig. 27 but for lithium.

reproduce the data. It is surprising that in these calculations, a typical evaporation part is missing and may indicate the need for a normalisation factor. We then compare the model calculations with the experiment for larger angles in the case of α-particle emission. This is done in Fig. 30. An evaporation part is clearly missing in the experimental cross sections at larger angles. Energy cuts are due to the experimental setup. We therefore show the energy parts not covered by the present experiment as dotted curves. The comparison at 17° for the QMD model is the same as in Fig. 27, but now on a logarithmic scale. The larger width of the evaporation bump in the experiment compared to the calculation becomes now more evident. The sudden decrease of the experimental yield is again due to the imperfection of

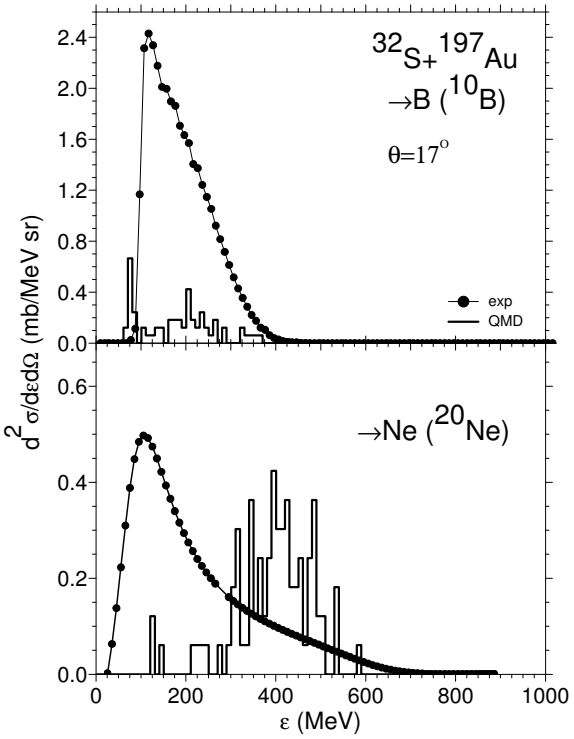

Fig. 29. The same as Fig. 27 but for boron (upper part) and neon (lower part). The calculations are for the isotopes given in brackets. The curves labelled 'exp' indicating the present work are the fits shown in Fig. 12.

the second detector as discussed above. For larger angles, the agreement between QMD calculation and the experimental results is moderate. When the SMM approach is added in the calculation (labelled QMD+SMM), the yield is reduced compared to the pure QMD calculation reducing the agreement even more.

Unfortunately, PHITS does not allow to vary certain model parameters which might improve the theoretical results. Also in Refs. [45] and [46], QMD calculations failed to reproduce experiments. This failure was overcome by treating the fermionic nature of the nucleons.

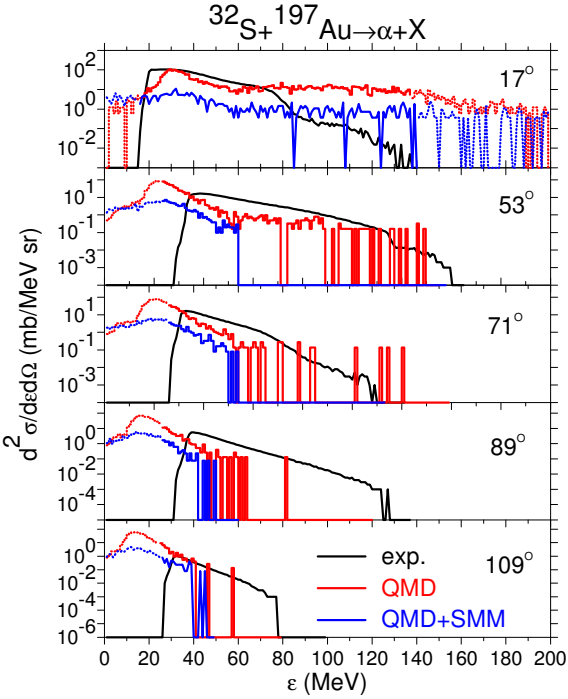

Fig. 30. (Colour on-line) Comparison of the double differential cross sections for the emission of helium at the indicated angles. The experiments shown as thick lines are for all helium isotopes, while the calculations are shown as thin histograms and are only for ^{4}He. The calculations outside the acceptance of the present experiment are shown as dotted curves. Calculations employing QMD are shown in light grey/red, while those employing QMD plus SMM are shown in dark grey/blue.

4. Summary

In the present work, we extend our studies in sulphur-induced reactions at 30 MeV A. In a first publication, we had presented charge correlations for ^{32}S+^{109}Ag and ^{32}S+^{197}Au [14]. These studies were supplemented by coincidence measurements for the reaction ^{16}O+^{197}Au at the same energy per nucleon [15]. From these coincidence measurements, we concluded that there is a strong correlation between two fragments when one of them is emitted in an angular range below the grazing angle. Otherwise, the emission is purely statistical. In a further study of ^{32}S+^{51}V, ^{109}Ag and^{238}U, we could test series of fragment emission models [16]. In the present paper, we study the reaction ^{32}S+^{197}Au. Since the data in Ref. [16] suffer from a rather high-energy threshold, in the present study we have lowered this threshold by adding a gas filled ionisation chamber to the solid state

telescope. Unfortunately, this became operational only at an angle of 17°. Energy spectra with similar threshold as before [16] were obtained at 53°, 71°, 89° and 107°. The advantage of a low-energy threshold has to be paid by poor particle resolution. Our present data allowed only to deduce energy integrated cross sections $\mathrm{d}\sigma/\mathrm{d}\Omega(Z,\vartheta)$. It was therefore impossible to test again the coalescence model which showed excellent reproduction of fragment spectra [16].

The energy spectra at 17° showed a component from projectile fragmentation. This is in agreement with the previous result from the uranium target and those for gold [24, 25, 29].

The GMSM model and its parameters deduced mainly in [16] were used to obtain angle integrated cross sections $\sigma(Z)$. The values are in agreement with the cross sections reported by [24, 25, 29] except for a valley around $Z = 18$.

A previously reported odd–even staggering [32, 33] could not be confirmed, most probably due to the large fraction of the cross sections stemming from evaporation from a fully equilibrated source.

Energy spectra or fragments were compared with QMD model [39–41] calculations. While alpha-particle emission seems to be appropriately reproduced, the calculations fail to do so for heavier fragments. However, calculations for energy and angle integrated cross sections agree with the experiments. Even the minimum around $Z = 18$ is reproduced. Calculations within the statistical multi-fragmentation model (SMM) [1, 2] give the general trend of the fragment distribution although only on a relative basis. However, when this approach follows after the QMD equilibration stage and before a standard evaporation-fission stage, as it is incorporated in the new PHITS code, agreement between experimental observables and model calculation becomes worse. The prediction of a relativistic version of the QMD model fails to reproduce the experiment.

The authors are grateful to the electronic workshop of IKP for help in setting up the start detector, the detector laboratory for preparing the Si(Li) detectors, the accelerator crew for preparing the excellent heavy-ion beams. Discussions with F. Hinterberger, J. Niskanen and C. Wilkin were found very helpful. Thanks goes to the anonymous referee for helping us to improve the publication. Two of us (H.M. and T.K.) thank the IKP of FZ Jülich for hospitality.

REFERENCES

[1] J.P. Bondorf *et al.*, *Phys. Rep.* **257**, 133 (1995).
[2] D.H.E. Gross, *Phys. Rep.* **279**, 119 (1997).

[3] K. Paech, W. Bauer, S. Pratt, *Phys. Rev. C* **76**, 054603 (2007).
[4] M.E. Fisher, *Rep. Prog. Phys.* **30**, 615 (1967).
[5] A.S. Hirsch *et al.*, *Phys. Rev. C* **29**, 508 (1984).
[6] C. Hartnack *et al.*, *Eur. Phys. J. A* **1**, 151 (1998).
[7] Qingfeng Li *et al.*, *J. Phys. G* **32**, 151 (2006).
[8] G.F. Bertsch, H. Kruse, S. Das Gupta, *Phys. Rev. C* **29**, 673(R) (1984).
[9] T. Gaitanos, H. Lenske, U. Mosel, *Prog. Part. Nucl. Phys.* **62**, 439 (2009).
[10] R.T. de Souza *et al.*, *Nucl. Instrum. Methods Phys. Res. A* **295**, 109 (1990).
[11] R.T. de Souza, N. Le Neindre, A. Pagano, K.-H. Schmidt, *Eur. Phys. J. A* **30**, 275 (2006).
[12] C.M. Herbach *et al.*, *Nucl. Instrum. Methods Phys. Res. A* **508**, 315 (2003).
[13] R. Barna *et al.*, *Nucl. Instrum. Methods Phys. Res. A* **519**, 610 (2004).
[14] H. Machner *et al.*, *Prog. Part. Nucl. Phys.* **62**, 413 (2009).
[15] J. Rama Rao *et al.*, *Eur. Phys. J. A* **38**, 35 (2008).
[16] H. Machner, M. Nolte, M. Palarczyk, T. Kutsarova, *Eur. Phys. J. A* **51**, 146 (2015).
[17] N. Le Neindre *et al.*, *Nucl. Instrum. Methods Phys. Res. A* **490**, 251 (2002).
[18] S. Barlini *et al.* [FAZIA Collaboration], *Phys. Rev. C* **87**, 054607 (2013).
[19] R. Bougault *et al.*, *Eur. Phys. J. A* **50**, 47 (2014).
[20] G. Pasquali *et al.* [FAZIA Collaboration], *Eur. Phys. J. A* **50**, 86 (2014).
[21] S. Wuenschel *et al.*, *Nucl. Instrum. Methods Phys. Res. A* **604**, 578 (2009).
[22] J.F. Ziegler, J.P. Biersack, `www.srim.org`, Programme SRIM, 2003.
[23] F. Hubert, A. Fleury, R. Bimbot, D. Gardes, *Ann. Phys.* **5**, 1 (1980).
[24] U. Milkau, Technical Report GSI-91-34, GSI, 1991.
[25] U. Milkau *et al.*, *Phys. Rev. C* **44**, R1242(R) (1991).
[26] H. Machner, *Z. Phys. A* **336**, 209 (1990).
[27] H. Machner *et al.*, *Prog. Part. Nucl. Phys.* **62**, 413 (2008).
[28] H. Machner, B. Razen, *Nucl. Instrum. Methods Phys. Res. A* **437**, 419 (1999).
[29] A. Lleres *et al.*, *Phys. Lett. B* **185**, 336 (1987).
[30] Y.D. Kim *et al.*, *Phys. Rev. C* **45**, 338 (1992).
[31] H. Machner *et al.*, *Phys. Rev. C* **73**, 044606 (2006).
[32] M. D'Agostino *et al.*, *Nucl. Phys. A* **861**, 47 (2011).
[33] G. Casini *et al.*, *Phys. Rev. C* **86**, 011602(R) (2012).
[34] R. Donangelo, K. Sneppen, S.R. Souza, *Comput. Phys. Commun.* **140**, 405 (2001).
[35] K.J. Le Couteur, D.W. Lang, *Nucl. Phys.* **13**, 32 (1959).
[36] U. Facchini, M.G. Marcazzan, L. Milazzo-Colli, E. Saetta-Menichella, *Phys. Lett. B* **26**, 278 (1968).

[37] S. Shlomo, J.B. Natowitz, *Phys. Lett. B* **252**, 187 (1990).
[38] J. Aichelin, *Phys. Rep.* **202**, 233 (1991).
[39] K. Niita *et al.*, *Phys. Rev. C* **52**, 2620 (1995).
[40] K. Niita *et al.*, *Radiat. Meas.* **41**, 1080 (2006).
[41] Y. Sawada *et al.*, *Nucl. Instrum. Methods Phys. Res. B* **291**, 38 (2012).
[42] S. Furihata, *Nucl. Instrum. Methods Phys. Res. B* **171**, 251 (2000).
[43] T. Ogawa, T. Sato, S. Hashimoto, K. Niita, *Nucl. Instrum. Methods Phys. Res. A* **723**, 36 (2013).
[44] D. Mancusi, K. Niita, T. Maruyama, L. Sihver, *Phys. Rev. C* **79**, 014614 (2009).
[45] M. Papa, T. Maruyama, A. Bonasera, *Phys. Rev. C* **64**, 024612 (2001).
[46] A. Ono, H. Horiuchi, *Prog. Part. Nucl. Phys.* **53**, 501 (2004).